 doi:10.20944/preprints202010.0435.v1

Article

Build Strategy and Impact Strength of SLM Produced Maraging Steel (1.2709)

Anders E. W. Jarfors [1,*], Akash Chikke Gowda Hosapalya Shashidhar [2], Hrushi Kailash Yepur [3] Jacob Steggo [4], Nils-Eric Andersson [5] and Roland Stolt [6]

[1] Jönköping University, School of Engineering, Deapartment of Materials and Manufacturing, Box 1026, 551 11 Jönköping, Sweden; anders.jarfors@ju.se
[2] Jönköping University, School of Engineering, Department of Materials and Manufacturing, Box 1026, 551 11 Jönköping, Sweden; hoak18ga@student.ju.se
[3] Jönköping University, School of Engineering, Department of Materials and Manufacturing, Box 1026, 551 11 Jönköping, Sweden; yehr18po@student.ju.se
[4] Jönköping University, School of Engineering, Department of Materials and Manufacturing, Box 1026, 551 11 Jönköping, Sweden; jacob.steggo@ju.se
[5] Jönköping University, School of Engineering, Department of Materials and Manufacturing, Box 1026, 551 11 Jönköping, Sweden; nils-eric.andersson@ju.se
[6] Jönköping University, School of Engineering, Department of Product Development, Box 1026, 551 11 Jönköping, Sweden; roland.stolt@ju.se
* Correspondence: anders.jarfors@ju.se

Abstract: The current paper aims to study the impact properties of additively manufactured Maraging steel (1.2709) using laser powder bed fusion (PBF-L) processing. The specimens were manufactured using 3Dsystems ProX 300 equipment under constant specific power input, or Andrew Number. The interactions between the build strategy and parameters, such as Hatch spacing and Scan speed was, and the impact strength and fracture were investigated. The Impact energy anisotropy was also investigated parallel and perpendicular to the build direction. Instrumented impact testing was performed, and the fractography supported that the fusion zone geometry dictated the fracture behaviour. The influence from gaseous elements such as Nitrogen, Oxygen and Hydrogen was found insignificant at the levels found in the printed material.

Keywords: Additive Manufacturing, Impact energy, Fracture, Hatch Spacing, Scan Speed, Process Parameters

1. Introduction

Additive manufacturing (AM) is one of the trending technologies for the manufacturing of parts, products, and assemblies with complex geometries and a great degree of design freedom. [1] AM produced may display greater strength, but this may be associated with a reduction of ductility and toughness [2].

Maraging steels are regarded as well-suited for Selective Laser Melting (SLM). Firstly, AM produced Maraging steels have a martensitic matrix, and the SLM processes provide rapid solidification and cooling. Secondly, Maraging steels are commonly used in aerospace and tooling industries due to the mechanical properties and that the AM process offers suitable capabilities for the limited series size and necessary geometry capability [3].

SLM processing involves several processes, properties and variables. The metal powder is spread in a layer with a certain thickness or build-height, typically 30-50µm and influence the quality significantly [4]. Oxidation of the material during SLM processing is managed by allowing an inert gas flowing over the powder bed, such as Argon and nitrogen Takata[5].

A simplistic approach to understanding how a dense material has been adopted by for instance Ciurana et al. [6] and De Souza et al. [7] This approach was based on the Volumetric specific energy

Preprints (www.preprints.org) | NOT PEER-REVIEWED | Posted: 21 October 2020 doi:10.20944/preprints202010.0435.v1

or Andrew number, E_d, that combines Laser power, P, Scan speed, v, Hatch spacing, h, and Build height, δ, as:

$$E_d = \frac{P}{vh\delta} \quad (1)$$

The basic process parameters are necessary for an internally sound product but not sufficient as there is significant complexities in the laser material and substrate interaction as well as a strong influence from the thermal history of the previously built layers. The selection of beam paths or scan strategy controls the quality of the part, influences the tensile properties, surface finish, and microstructure [8]. There are many different strategies possible:

- **Island Strategy:** Each layer is divided into smaller regions and scanned in different orientations in a random order, Figure 1a. The island grid is translated after completion of each successive built layer by 1mm to manage residual stress and thus deformation and cracking [9]. The island strategy creates the weld lines between the islands on the part surface. To reduce anisotropy, residual stress and crystallographic texture, the interlayer scanning direction are also typically rotated 67 or 90 degrees, keeping hatch spacing and line scanning relation to the adjacent slice layer constant [8].
- **Spiral Scanning strategy:** The beam pat creates a spiral helical pattern, Figure 1b. Helical scanning avoids overheating near the sides of the printed part. Typically this requires high power and high laser scan speed laser ensure good interlayer bonding[10]. A drawback is an increased risk of overheating in the centre of the part [8,10].
- **Chessboard scan strategy:** The print area is divided into smaller square regions, scanned in a sequence with "white square" scanned first, followed by "black squares", figure 1c [11]. This is similar to the Island strategy but results n a more homogeneous bed heating [8].
- **Stripes scan strategy:** The scan pattern consists of a "band" of scan lines with the freedom of an interlayer rotation of 67 or 90 degrees. Residual stress is commonly lower in the chessboard strategy compared to the stripes scanning strategy, but results in a higher density for higher hatch distance and higher degree interlayer rotation, but may result in higher surface roughness compared to chessboard scan strategy but lesser than the hexagonal scan strategy [8].
- **Hexagonal scan strategy:** Hexagonal scan strategy is a variant of the Spiral scanning pattern and commonly has the option of scanning inside-out or outside-in. The hexagonal scan strategy typically results in a higher porosity compared to the stripes and chessboard scan strategy[8].

Preprints (www.preprints.org) | NOT PEER-REVIEWED | Posted: 21 October 2020 doi:10.20944/preprints202010.0435.v1

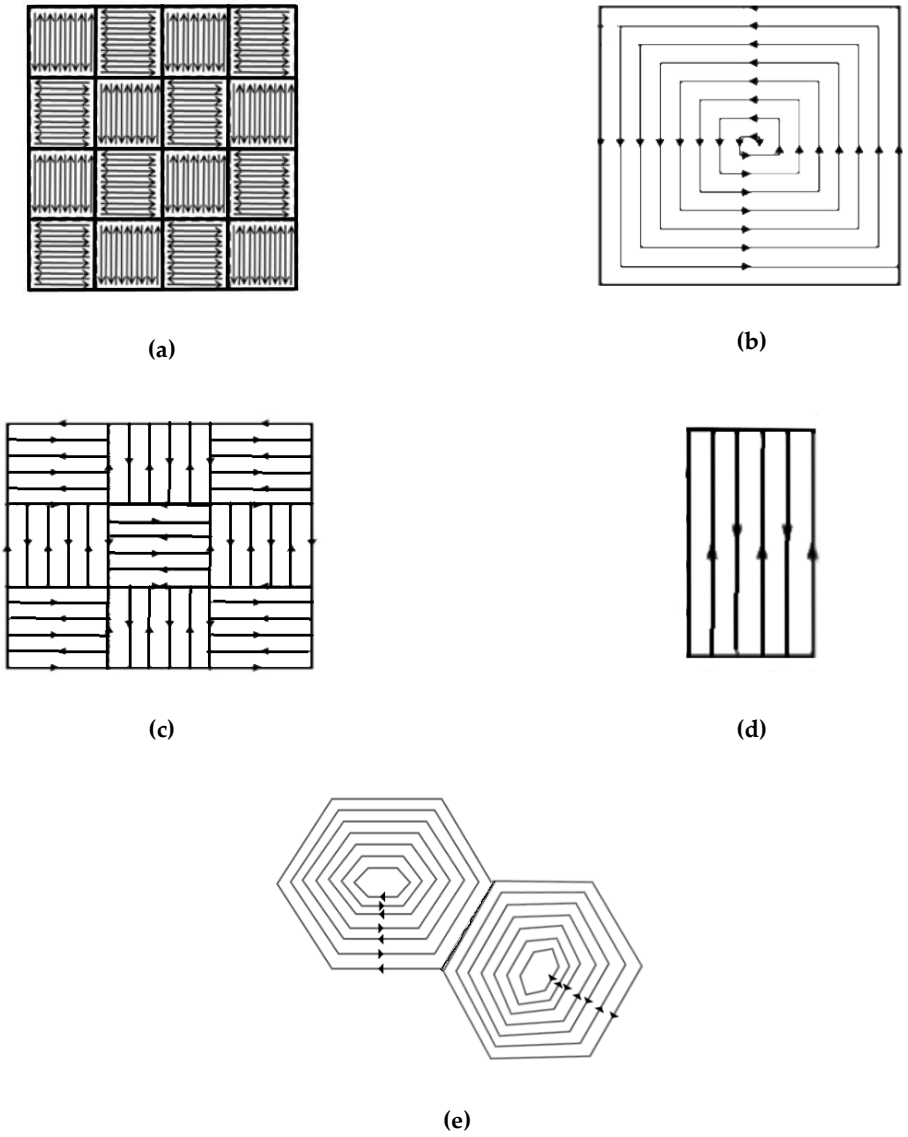

Figure 1. Scan strategies with (a) Island scanning strategy, (b) Spriral scanning strategy, (c) Chessboard scanning strategy, (d) Stripes scanning strategy, and (e) Hexagonal scanning strategy.

The low carbon content of the Maraging steel 1.2709 decreases the risk of quench cracking, while the high nickel increases the risk. Under normal conditions, Maraging steel 1.2709 displays excellent t toughness [12]. As with high strength steels, hydrogen embrittlement is a risk. The management of Hydrogen and Oxygen in AM-process has not been the primary focus for the developers and the powders, and the handling commonly results in relatively high levels of impurities. Similarly, the proactive atmosphere is often Nitrogen for SLM processing, and the nitrogen content has been given little focus as well. The matrix lath martensite is also increasing the sensitivity to the hydrogen embrittlement[13].

In steel research, there has been a strong research activity bringing down the oxygen content, both dissolved and in the form of non-metallic inclusions, combined with inclusion morphology management. [14]oxygen is also highly detrimental to toughness and impact strength of in welded steel [15] and oxygen levels below 400ppm are normally required for high strength steel [16]. It should be noted that for low strength steel, a low oxygen content does not necessarily result in high

Preprints (www.preprints.org) | NOT PEER-REVIEWED | Posted: 21 October 2020 doi:10.20944/preprints202010.0435.v1

toughness, partially due to the martensite transformation and interactions with the Oxygen, especially in welded materials. [16] In the case of Maraging steel, a reduction of N and O gases dissolved in the with 40% reduces the amounts of inclusions by 30%. The reduction of the inclusions and dissolved Oxygen and Nitrogen increased both ductility and impact energy with up to 40% for levels well below 200ppm[17].

Important to understand is that the fracture behaviour is strongly affected by the effect of build orientation, resulting in an anisotropic microstructure and this also anisotropic mechanical properties. Fracture of AM materials are often strongly influenced by pre-existing defects, such as unmelted powder particles, splats from spatter, cavities originated by incomplete fusion between layers and tracks. [4]

The force-displacement behaviour during impact testing has a generic appearance, as shown in figure 2. The curve displays some specific features with the characteristic points identified as [18].

- F_{dy} = dynamic yield force
- F_m = maximum force
- F_{ci} = crack initiation force
- F_a = crack arrest force

The events during the impact test start with an elastic response until the dynamic yield force, F_{dy} is reached, Once the material yields it will begin to harden until the maximum force is reached, F_m, The next event will be crack initiation. This may be preceded by dynamic softening and as such, the crack initiation force, F_{ci}, is the same or lower than the maximum force, F_m, After crack initiation a crack will form and propagate under stable conditions as the force is reduced from, F_{ci}, down to F_a, which is the crack arrest point [18].

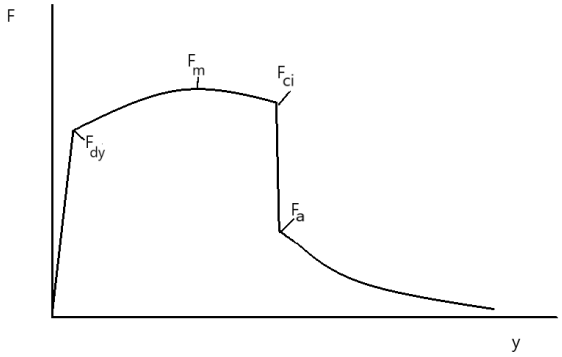

Figure 2. Schematic illustration of the characteristics of the force-displacement curve for an instrumented Charpy-V tests freely after ref. [18]

The current paper aims to investigate the impact fracture strength and crack propagation characteristics of Maraging steel 1.2709 as well as to establish the level of Oxygen, Hydrogen and nitrogen content in this material. The influence of the scan pattern on fracture strength and performance as well as if there is any relation to the content of Hydrogen, Nitrogen and Oxygen.

2. Materials and Methods

2.1 Materials processing

The studied material, Maraging steel 1.2709, was printed using the SLM system ProX 300 by 3DSystems. The printing parameter variation was made in such a way that the known conditions for a full density material were taken with a specific energy density or Andrew number of 89 J/mm^3. The standard build height of 40µm was also used. The influence of Laser fluence was unchanged as a constant laser power of 159 W was used. The variation in the current study was the laser scan speed

Preprints (www.preprints.org) | NOT PEER-REVIEWED | Posted: 21 October 2020 doi:10.20944/preprints202010.0435.v1

and the hatch spacing that were varied in such a way to keep the Andrew number constant. The scan strategy in the form of a Stripe, Chessboard and Hexagonal scanning patter together with a variation of the interlayer scanning rotation was used as variables with the settings collated in Table 1.

Table 1. Process parameter setting for the experiments made.

Stripes	**E (J/mm³)**	**P(W)**	**V(mm/s)**	**H(mm)**	**Deg (°)**
Family 1	89	159.36	994.76	0.045	90
Family 2	89	159.36	596.85	0.075	90
Family 3	89	159.36	746.07	0.060	90
Chessboard	**E (J/mm³)**	**P(W)**	**V(mm/s)**	**H(mm)**	**Deg (°)**
Family 1	89	159.36	994.76	0.045	45
Family 2	89	159.36	596.85	0.075	45
Family 3	89	159.36	746.07	0.060	45
Stripes	**E (J/mm³)**	**P(W)**	**V(mm/s)**	**H(mm)**	**Deg (°)**
Family 1	89	159.36	994.76	0.045	45
Family 2	89	159.36	596.85	0.075	45
Family 3	89	159.36	746.07	0.060	45

2.2 Oxygen and Nitrogen measurement

Oxygen, Nitrogen and Hydrogen content in the printed state was measured using an ELTRA ONH-200 using Nitrogen or Helium as the carrier gas depending on the species being analysed.

2.3 Instrumented Charpy-V testing

To characterise the impact strength properties of the printed samples. The samples in each family are tested with the impact direction parallel and perpendicular to the build direction as a test of anisotropy. Each family consisted of three samples with two samples in each family are tested in the parallel direction, and one sample in the perpendicular direction.

The V-shaped notch was cut from the printed square bars. The samples are marked for the notch in the centre of the Charpy face. The face that is selected for the notch is based on the built direction and parallel or perpendicular. For the test in the parallel direction, the impact was made on the side from which the support structure had been remove as tensile stress would develop on the opposite face which then was in the as-printed state.

The instrumentation consisted of accelerometers and an angular attitude meter. The total energy was established through the angular rotation, and the accelerometer data was normalised against this total energy to provide force-displacement data, using a dedicated MATLAB code.

2.4 Fractography

A selection of the fractured samples was studied under a JEOL JSM7001F scanning electron microscope (SEM) to investigate the nature of the fracture surfaces.

3. Results and discussion

3.1 Oxygen and Nitrogen measurement

The gas content was analysed from one sample from processing family and as a total of nine different samples, were tested. Since all samples were printed simultaneously, the only cause of a variation would be the print strategy and process settings (Hatch spacing and Scan speed).

The first observation was that Hydrogen appeared not to be an issue as the hydrogen content was below the detection limit of the instrument, and no meaningful results could be obtained.

Preprints (www.preprints.org) | NOT PEER-REVIEWED | Posted: 21 October 2020 doi:10.20944/preprints202010.0435.v1

Oxygen and Nitrogen, on the other hand, were possible to measure and showed significant amounts in the printed state, Table 2. ANOVA analysis was made to identify any statistically significant relationship between build strategy and process parameters. This was not possible, and under the current conditions, the gas content was deemed independent on build strategy and process parameters. From Table 2, it can, however, be observed that there appears to be a tendency for both the Oxygen and Nitrogen content to be lower than for the other strategies.

Table 2. Process parameter and gas content.

SL NO	Build Strategy	V(mm/s)	H(mm)	DEG (°)	Oxygen (ppm.)	Nitrogen (ppm.)
1	Stripes	994.76	0.045	90		
2	Stripes	994.76	0.045	90	1467.64	252.73
3	Stripes	994.76	0.045	90		
4	Stripes	596.85	0.075	90		
5	Stripes	596.85	0.075	90	1133.34	218.17
6	Stripes	596.85	0.075	90		
7	Stripes	746.07	0.06	90		
8	Stripes	746.07	0.06	90	1029.63	248.91
9	Stripes	746.07	0.06	90		
10	Chessboard	994.76	0.045	45		
11	Chessboard	994.76	0.045	45	992.12	202.67
12	Chessboard	994.76	0.045	45		
13	Chessboard	596.85	0.075	45		
14	Chessboard	596.85	0.075	45	1072.88	205.99
15	Chessboard	596.85	0.075	45		
16	Chessboard	746.07	0.06	45		
17	Chessboard	746.07	0.06	45	971.05	252.32
18	Chessboard	746.07	0.06	45		
19	Hexagon	994.76	0.045	45		
20	Hexagon	994.76	0.045	45	1110.92	256.28
21	Hexagon	994.76	0.045	45		
22	Hexagon	596.85	0.075	45		
23	Hexagon	596.85	0.075	45	1109.11	213.99
24	Hexagon	596.85	0.075	45		
25	Hexagon	746.07	0.06	45		
26	Hexagon	756.07	0.06	45	1179.82	207.59
27	Hexagon	746.07	0.06	45		

3.2 Instrumented Charpy-V testing

The results from the instrumented Charpy-V testing are collated in Table 3. Figure 3 shows an example of a force-displacement curve.

The chessboard pattern, row 14 (laser power 596.85mm/s, hatch spacing 0.075mm, and degree of interlayer rotation 45) in the parallel direction of the impact parallel to the build direction showed the highest impact strength. The maximum force was of 15000N, which was very different from the other samples. Otherwise, the average impact strength for the stirpes strategy was 20J, and for the chessboard family 29J. The hexagonal strategy gave an average of 21J with the settings used. This suggests that the Chessboard produced the best toughness on average.

All the other built strategy samples show similar behaviour for their impact strength of the material. So, the displacement vs time graph of the highest and lowest impact strength of each built strategy family is shown below, where we can evaluate the maximum load point.

Table 3. Process parameter setting for the experiments made.

Preprints (www.preprints.org) | NOT PEER-REVIEWED | Posted: 21 October 2020 doi:10.20944/preprints202010.0435.v1

Row no	Build Strategy	V (mm/s)	H (mm)	DEG (°)	Impact Direction	Impact Strength (J)	F_{dy} (N)	F_m (N)	F_{ci} (N)	F_{ca} (N)
1	Stripes	994.76	0.045	90	Parallel	17.6	2520	2890	2425	720
2	Stripes	994.76	0.045	90	Parallel	-				
3	Stripes	994.76	0.045	90	Perpendicular	17	2110	2180	1950	820
4	Stripes	596.85	0.075	90	Parallel	18.5	1970	2095	1970	780
5	Stripes	596.85	0.075	90	Parallel	19.8	2100	2830	2100	680
6	Stripes	596.85	0.075	90	Perpendicular	15.9	2550	2600	2240	700
7	Stripes	746.07	0.06	90	Parallel	26.3	2380	2730	2250	1120
8	Stripes	746.07	0.06	90	Parallel	26.2	3200	3720	3120	900
9	Stripes	746.07	0.06	90	Perpendicular	18.7	2370	2750	2280	1110
10	Chessboard	994.76	0.045	45	Parallel	21.7	1150	1720	1550	1210
11	Chessboard	994.76	0.045	45	Parallel	19.8	2070	2110	1440	800
12	Chessboard	994.76	0.045	45	Perpendicular	16.3	2310	2315	2185	520
13	Chessboard	596.85	0.075	45	Parallel	-				
14	Chessboard	596.85	0.075	45	Parallel	55.5	12000	15000	13000	4500
15	Chessboard	596.85	0.075	45	Perpendicular	-				
16	Chessboard	746.07	0.06	45	Parallel	35.8	2800	4180	3500	1175
17	Chessboard	746.07	0.06	45	Parallel	27.6	2100	2150	2050	510
18	Chessboard	746.07	0.06	45	Perpendicular	25	3500	3500	3400	1120
19	Hexagon	994.76	0.045	45	Parallel	-				
20	Hexagon	994.76	0.045	45	Parallel	19.7				
21	Hexagon	994.76	0.045	45	Perpendicular	14.7	752	1156	967	237
22	Hexagon	596.85	0.075	45	Parallel	-				
23	Hexagon	596.85	0.075	45	Parallel	18.2	1250	1321	1100	356
24	Hexagon	596.85	0.075	45	Perpendicular	29	1780	2300	1750	600
25	Hexagon	746.07	0.06	45	Parallel	21.2	1000	1851	1400	470
26	Hexagon	756.07	0.06	45	Parallel	20	1000	1771	1400	255
27	Hexagon	746.07	0.06	45	Perpendicular	22.4	1500	2409	1837	921

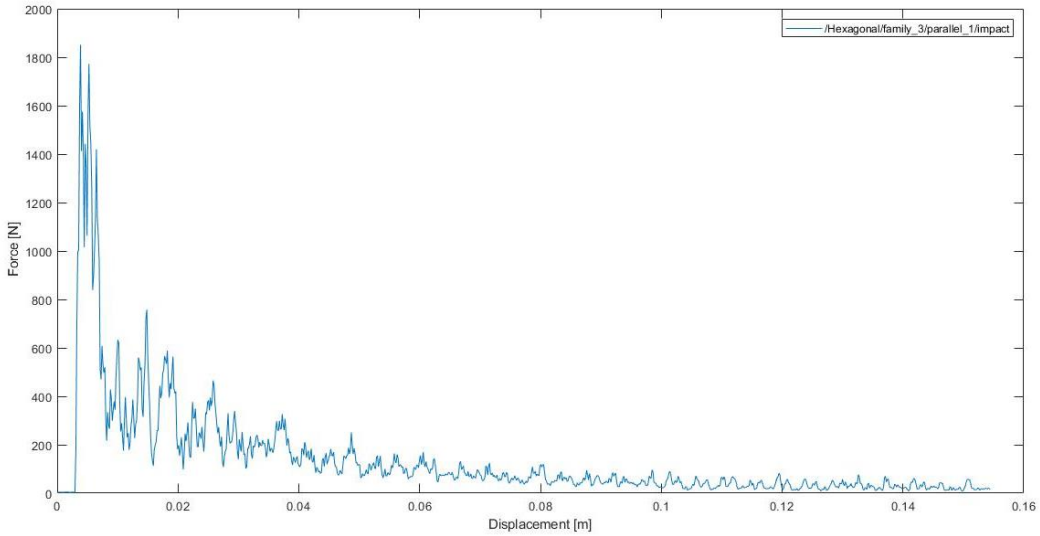

Figure 1: Load versus displacement for Hexagonal family 3 with an impact direction parallel to the build direction.

Preprints (www.preprints.org) | NOT PEER-REVIEWED | Posted: 21 October 2020 doi:10.20944/preprints202010.0435.v1

3.4 ANOVA analysis of the Instrumented Charpy-V testing

3.4.1 Impact energy

A regression analysis, together with ANOVA analysis, allowed for a model to be built, Table 4a. The Model F-value of 12.88 implied the model was significant as there is only a 0.01% chance that an F-value this large could occur due to noise. The P-values show the influence of the individual influence from the parameters. A P-value of less than 0.0500 indicates model terms were significant. In this case, A-Hatch spacing, B-Inter layer rotation, C-Build strategy, and E-Direction of impact. In addition to this AB, the interaction between Hatch spacing and Interlayer rotation was significant.

The Lack of Fit F-value of 4.09 implies there is a 6.69% chance that a Lack of Fit F-value this large could occur due to noise. This relatively low probability as normally values greater than 10% would be discriminating for the model) is troubling.

The regression model displays a quantitative capability as the signal to noise ratio, or Adeq Precision was 15.042, which is greater than the critical value of 4 indicates an adequate signal. This even though R^2 only is 0.8111, Table 4b.

The data set and the model was also analysed for Gaussian distribution of the residual around the model, which also was the case. The magnitude of the residuals was also independent of the predicted value. The existence of outliers was established using the Cooke's distance method. In the process of developing the model, it was also discovered that the best fit was to use the inverse square root transform of the model using the Box-Cox plot method.[19]

The resulting model was:

$$\frac{1}{\sqrt{Impact\ Strength}} = 0.2215 - 0.0183A + 0.0310B - 0.0238C(1) + 0.000C(2) + 0.0103E + 0.0200AB \quad \text{Eq. (1)}$$

where A: Hatch spacing (mm), B: interlayer rotation (°), C: scan strategy (C(1)=Stripes, (C(2)=Chessboard, C(3)=Hexagonal), E, Impact direction (°), AB is the interaction between A and B (Hatch spacing (mm) and interlayer rotation (°)).

Table 4a. ANOVA Output from for the Impact strength analysis using a reduced 2FI model with a transformed response using the inverse square root transform.

Source	Sum of Squares	df	Mean Square	F-value	p-value	
Model	0.0146	5	0.0029	12.88	< 0.0001	significant
A-H(mm)	0.0048	1	0.0048	21.33	0.0003	significant
B-DEG (◦)	0.0038	1	0.0038	16.57	0.0010	significant
C-Built strategy	0.0018	1	0.0018	7.80	0.0136	significant
E-Charpy test	0.0020	1	0.0020	8.87	0.0094	significant
AB	0.0044	1	0.0044	19.35	0.0005	significant
Residual	0.0034	15	0.0002			
Lack of Fit	0.0030	10	0.0003	4.09	0.0669	not significant
Pure Error	0.0004	5	0.0001			
Cor Total	0.0180	20				

Table 4b. Regression fitting parameters for the Impact strength analysis using a reduced 2FI model with a transformed response using the inverse square root transform.

Preprints (www.preprints.org) | NOT PEER-REVIEWED | Posted: 21 October 2020 doi:10.20944/preprints202010.0435.v1

Entity	Value	Entity	Value
Std. Dev.	0.0151	R^2	0.8111
Mean	0.2149	Adjusted R^2	0.7481
C.V. %	7.01	Predicted R^2	0.6395
		Model Precision	15.0422

The resulting model showed that the influence of the parameters was similar for the three different scanning strategies, but the actual magnitude was shifted with the average impact energy of 20.0 J. for the Stripes strategy, 28.8 J. for the Chessboard strategy and 20.7 J. for the Hexagonal strategy. Increasing hatch spacing improved impact strength for all cases, and smaller interlayer rotation was to prefer, Figure 4a-c. It should here be noted that these experiments were done under constant Andrew number, meaning that increasing hatch spacing also implies decreasing scan speed under the condition with continuous total heat input. It will, however, affect the heat distribution and thus also alter the martensite transformation as well as the melt boundaries or fusion lines in the build material.

The effect of the testing direction revealed that the direction of impact was parallel to the build direction the impact energy was slightly higher than when it was perpendicular using the average of overall build strategies, figure 5. AM results in a layered structure. Impact in the build direction will result in the layer are stretches and a propagating crack will have to propagate through a layer and then across the fusion line again and again in a series-coupled chain of events. In the case of a perpendicular impact, the crack propagation should propagate simultaneously in the build layer and the fusion zone. Assuming that the fusion zone has lower strength than the inside of the weld is tougher than the parallel impact should result in a tougher material with a higher impact strength which also was the case in the current study.

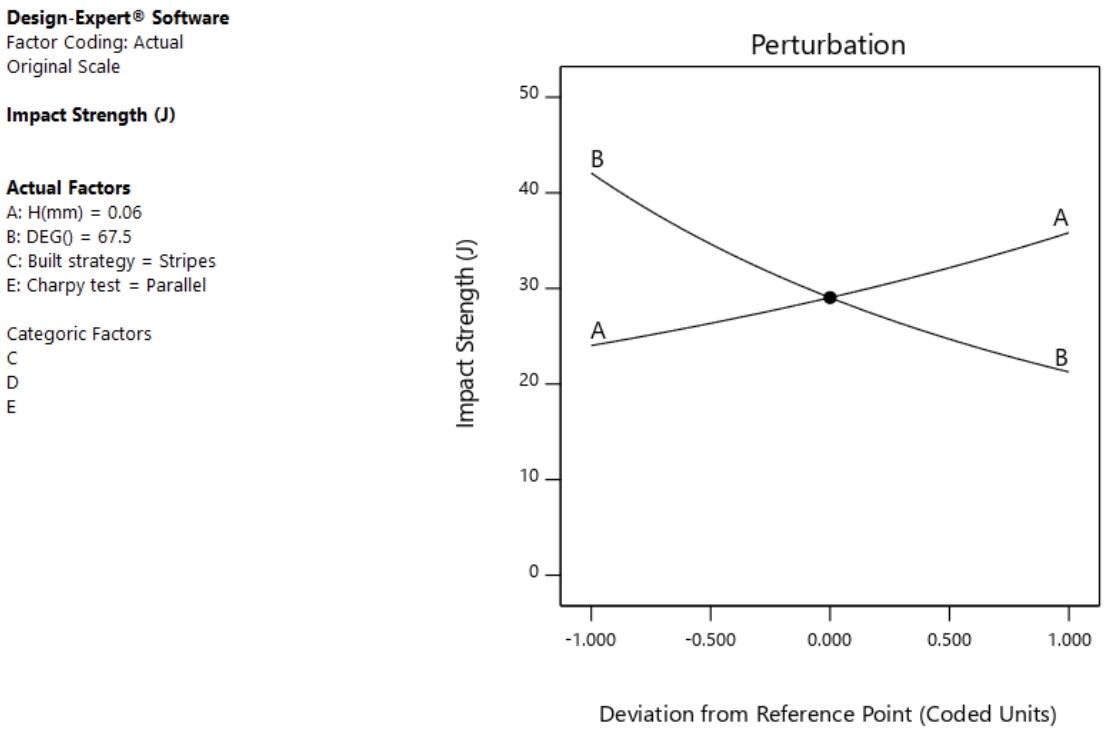

(a)

Preprints (www.preprints.org) | NOT PEER-REVIEWED | Posted: 21 October 2020 doi:10.20944/preprints202010.0435.v1

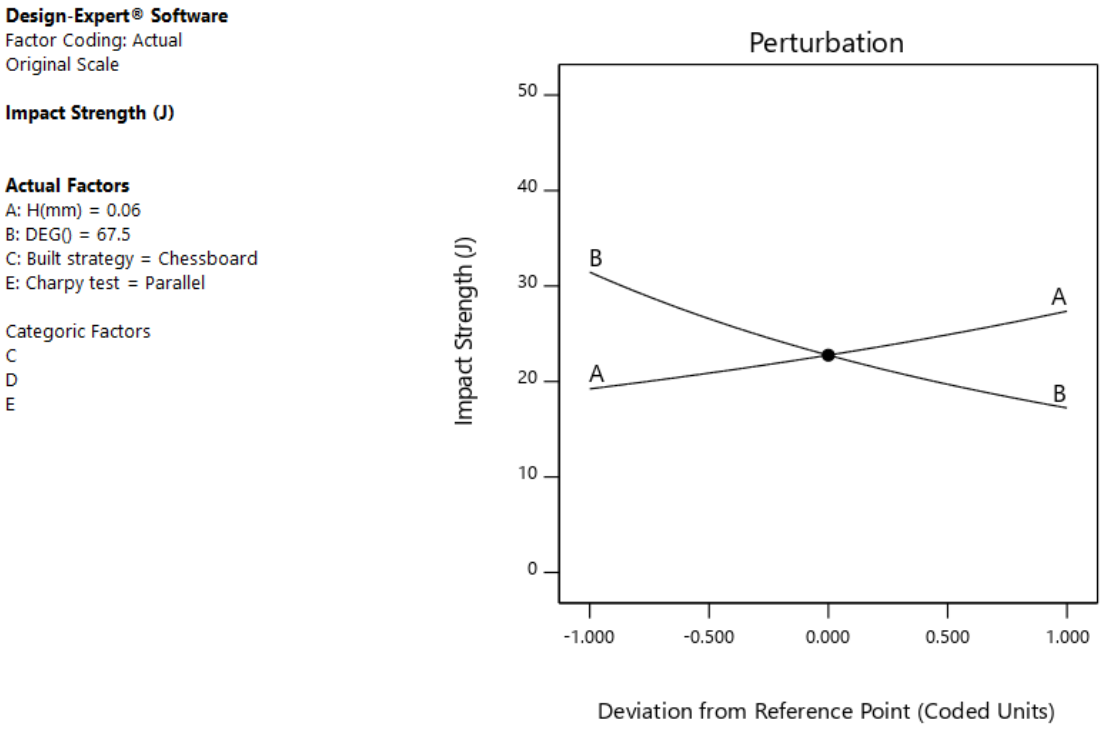

(b)

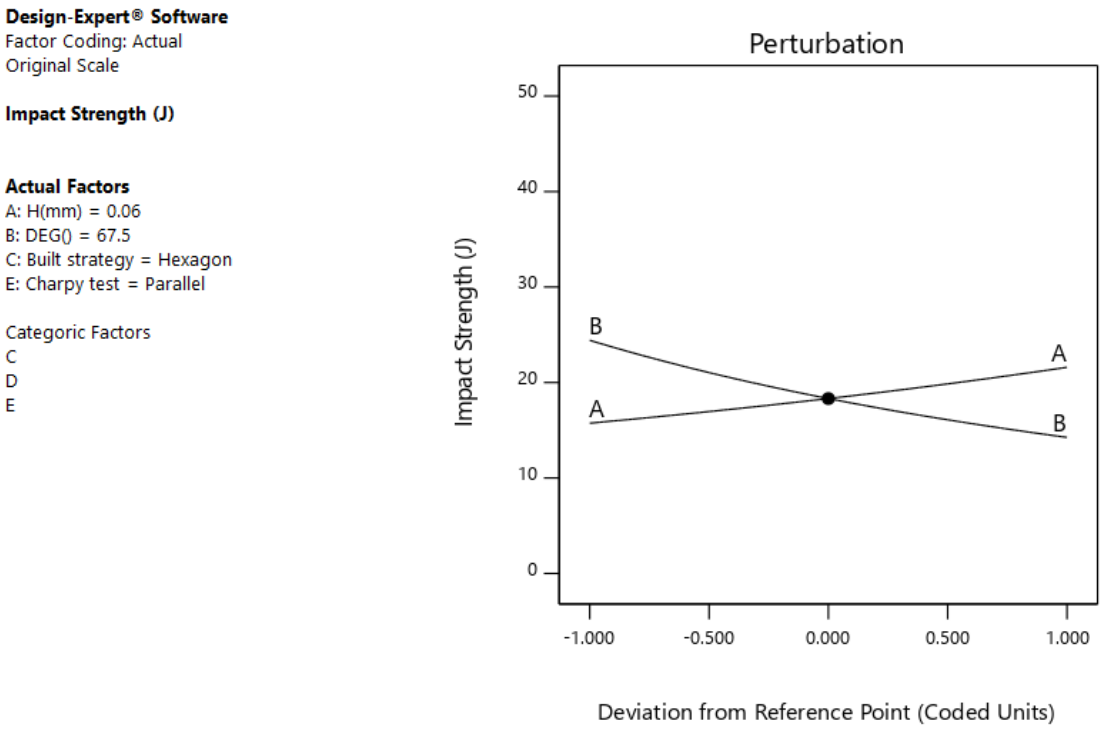

(c)

Figure 4. The influence of the process parameter for (a) Stripes scanning strategy, (b) Chessboard strategy, and (c) Hexagonal scanning strategy.

Preprints (www.preprints.org) | NOT PEER-REVIEWED | Posted: 21 October 2020 doi:10.20944/preprints202010.0435.v1

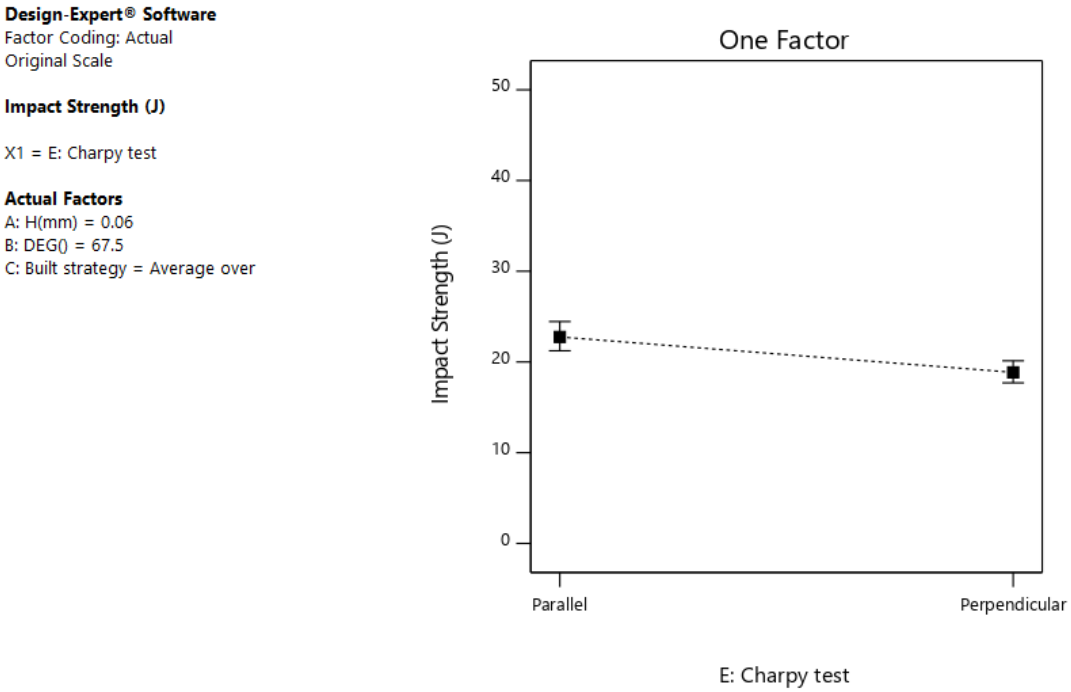

Figure 5: Variation of Impact strength with the direction of impact relative the build direction.

Preprints (www.preprints.org) | NOT PEER-REVIEWED | Posted: 21 October 2020 doi:10.20944/preprints202010.0435.v1

3.4.2 Forces

The limited number of experiments and the relatively high level of noise made the modelbuilding for the different forces on the impact curve difficult. Significant models for the dynamic yield point, maximum force and crack opening forces could not be generated. The crack arrest force was, however, possible to generate a model for, Table 5 a and 5b. The Model F-value of 5,89 implied the model was significant as there is only a 0.49% chance that an F-value this large could occur due to noise. The P-values show the influence of the individual influence from the parameters. Again a P-value of less than 0.0500 indicates model terms were significant; hence B-Inter layer rotation and C-Build strategy were significant. In addition to this AB, the interaction between Hatch spacing and Interlayer rotation was near significant, and thus A-Hatch spacing was kept to maintain the model hierarchy.

The Lack of Fit F-value of 1,29 implies there is a 41.34% chance that a Lack of Fit F-value this large could occur due to noise. This is not a low value, but it still validates the Lack of Fit as non-significant, which is a requirement.

The regression model displays a quantitative capability as the signal to noise ratio, or Adeq Precision was 9.2890, which is greater than the critical value of 4 indicates an adequate signal. This even though R^2 only is 0.5956, It should also be noted that the Predicted R^2 of 0.3403 is in reasonable agreement with the Adjusted R^2 of 0.4945; i.e. the difference is less than 0.2, Table 5b.

Table 5a. ANOVA Output from for the Impact strength analysis using a reduced 2FI model with a transformed response using the inverse square root transform.

Source	Sum of Squares	df	Mean Square	F-value	p-value	
Model	0.0016	4	0.0004	5.89	0.0041	significant
A-H(mm)	0.0002	1	0.0002	2.64	0.1235	hierarchy
B-DEG (◦)	0.0006	1	0.0006	8.87	0.0089	significant
C-Built strategy	0.0013	1	0.0013	19.77	0.0004	significant
AB	0.0002	1	0.0002	3.27	0.0892	Near significant
Residual	0.0011	16	0.0001			
Lack of Fit	0.0008	11	0.0001	1.29	0.4134	not significant
Pure Error	0.0003	5	0.0001			
Cor Total	0.0027	20				

Table 5b. Regression fitting parameters for the Impact strength analysis using a reduced 2FI model with a transformed response using the inverse square root transform.

Entity	Value	Entity	Value
Std. Dev.	0.0082	R^2	0.5956
Mean	0.0383	Adjusted R^2	0.4945
C.V. %	21.44	Predicted R^2	0.3403
		Model Precision	9.2890

The data set and the model was also analysed for Gaussian distribution of the residual around the model, which also was the case. The magnitude of the residuals was also independent of the predicted value. The existence of outliers was established using the Cooke's distance method. In the process of developing the model, it was also discovered that the best fit was to use the inverse square root transform of the model using the Box-Cox plot method which is the same as for the Impact energy.[19]

Preprints (www.preprints.org) | NOT PEER-REVIEWED | Posted: 21 October 2020 doi:10.20944/preprints202010.0435.v1

The resulting regression model was

$$\frac{1}{\sqrt{Cack\ Arrest\ Force}} = 0.0430 - 0.0043A + 0.0214B - 0.0214C(1) + 0.000C(2) + 0.0045AB$$

Eq. (2)

It should be noted that the values are in a coded mode for this case where the variables go from -1 to 1 in the investigated range, defined as Coded value= 2(Actual value – mid-range value)/(range). The average Ctrack arrest force for the different strategies was 854N for the Stripes strategy, 1405N for the Chessboard strategy and 473N for the Hexagonal strategy.

The Stripes build strategy shows a strong dependence on the process parameter A hatch spacing and B Interlayer rotation. It should here be noted that A was kept due to hierarchy as the interaction AB was significant. This is illustrated in figure 6a for the stripes strategy. Here a 90° interlayer rotation resulted in no dependence on the A hatch spacing. With a 45° interlayer rotation, this, on the other hand, resulted in a strong dependence, figure 6a. This was physically significant for the Stripes build strategy, figure 6b, whereas the effect for the Chessboard strategy, figure 6c and Heaxaginal strategy, figure 6e, was less evident. Important here to take note of is that the qualitative dependence of the Crack arrest force on the process parameters were the same as for that of the impact energy. The analysis of the Impact energy suggested that the impact energy were strongly dependent on the geometry of the fusion zone and the crack arrest forces suggest a similar dependence supporting that the fusion zone is dominant. This can be stated in the view that there was no such relationship found for neither Hydrogen nor Oxygen, which often are regarded as common causes of embrittlement.

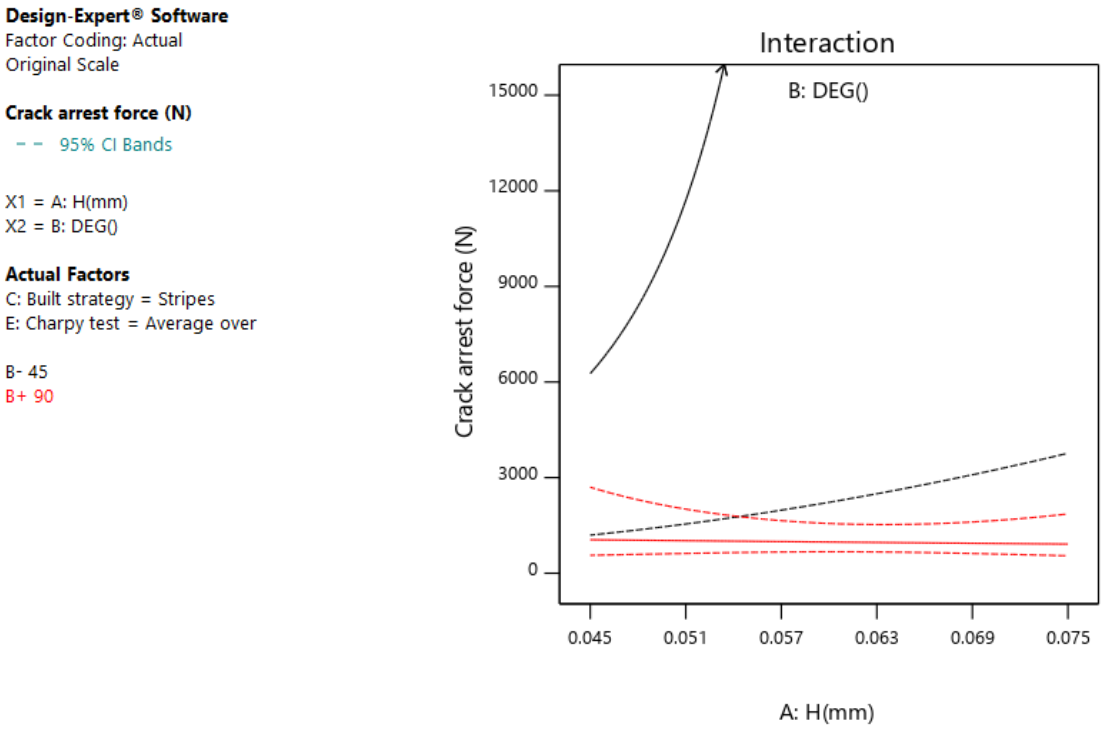

(a)

Preprints (www.preprints.org) | NOT PEER-REVIEWED | Posted: 21 October 2020 doi:10.20944/preprints202010.0435.v1

Design-Expert® Software
Factor Coding: Actual
Original Scale

Crack arrest force (N)

Actual Factors
A: H(mm) = 0.06
B: DEG() = 67.5
C: Built strategy = Stripes
E: Charpy test = Average over

Factors not in Model
E

Categoric Factors
C
D
E

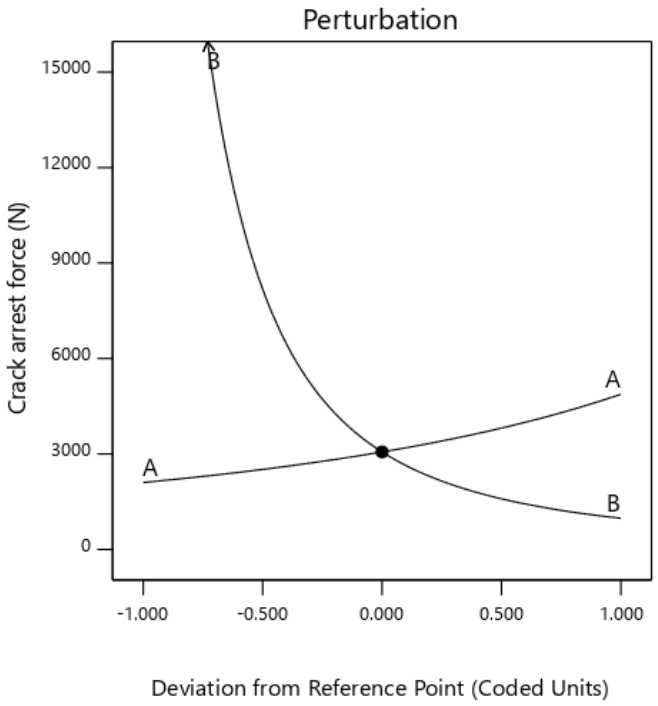

(b)

Design-Expert® Software
Factor Coding: Actual
Original Scale

Crack arrest force (N)

Actual Factors
A: H(mm) = 0.06
B: DEG() = 67.5
C: Built strategy = Chessboard
E: Charpy test = Average over

Factors not in Model
E

Categoric Factors
C
D
E

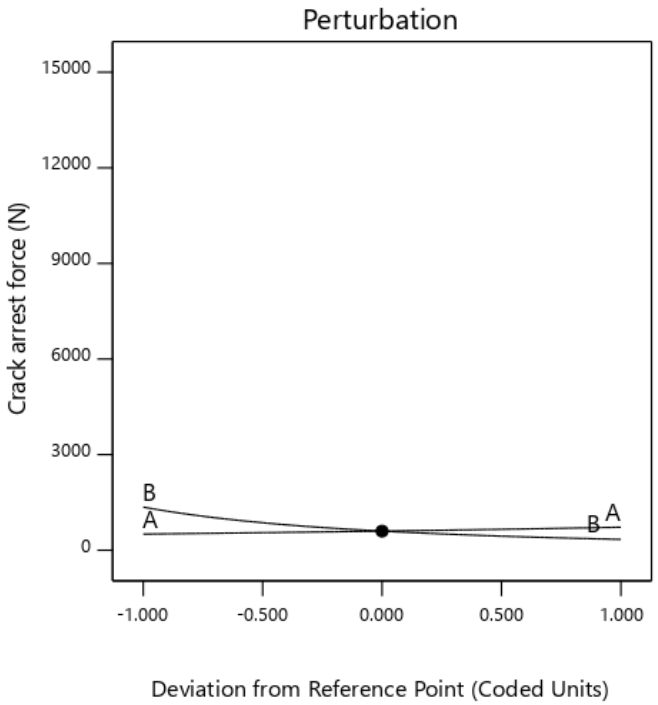

(c)

Preprints (www.preprints.org) | NOT PEER-REVIEWED | Posted: 21 October 2020 doi:10.20944/preprints202010.0435.v1

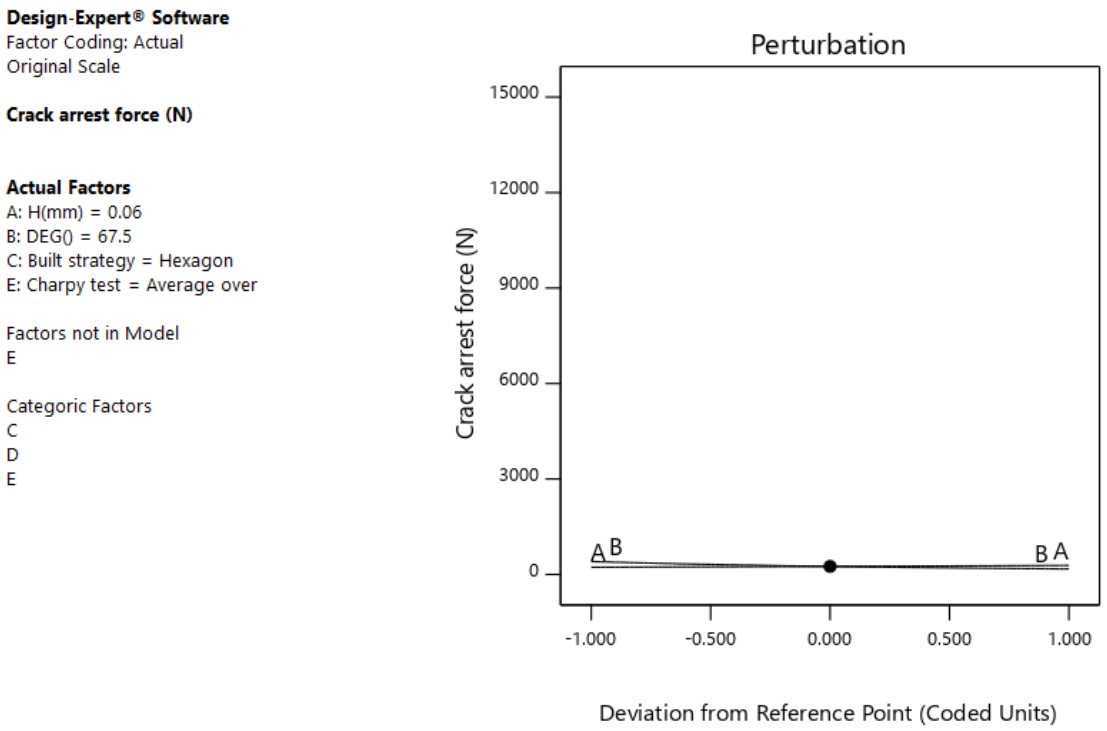

(d)

Figure 6. Process parameters on the Crack arrest force (a) The interaction between A Hatch spacing and B Interlayer rotation for the stripes strategy, (b) Perturbation plot for the Stripes build strategy (c) Perturbation plot for the Chessboard strategy, and (d) Perturbation plot for the Hexagonal scanning strategy

3.5 Fractography

The differences in crack propagation between the different build strategies were investigated through fractography. It should here be noted that all fractures were macroscopically brittle, which also is seen in the energy level with most of the tests resulted under 27J. Figure 7 shows the Fractured surface of a Chessboard family 1. This fracture surface shows a mixed-mode fracture on the microscopic level.

In figure 7a, the main feature is a smooth featured surface that is an oxidised surface surrounded by ductile features with ductile ridges and dimples. Dimples are also shown in figure 7b showing a clear ductile fracture in the matrix. The geometry and attributes correspond to typical defects related to defects in the fusion zone, suggesting a lack of fusion or severe oxidation as a base mechanism. In the fracture unmelted particles could also be found supporting that lack of fusion is if the driving element for the crack propagation, figure 7c.

Preprints (www.preprints.org) | NOT PEER-REVIEWED | Posted: 21 October 2020 doi:10.20944/preprints202010.0435.v1

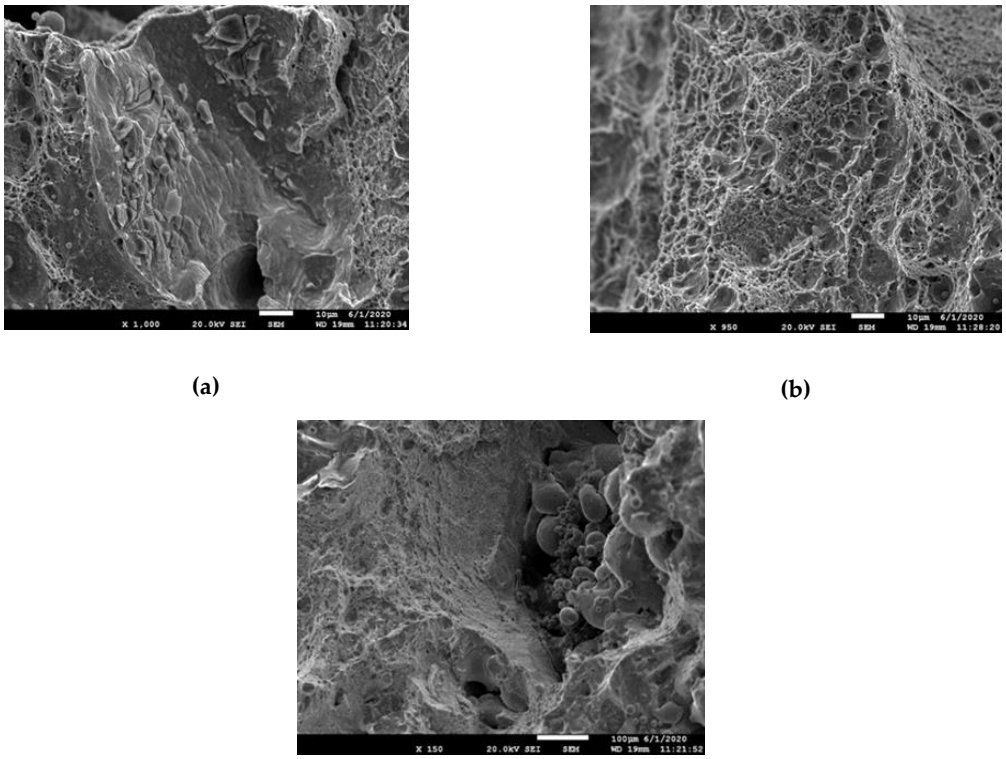

(a) **(b)**

(c)

Figure 7: The fractured surface of the Chessboard family 1 (Samples 10-12)

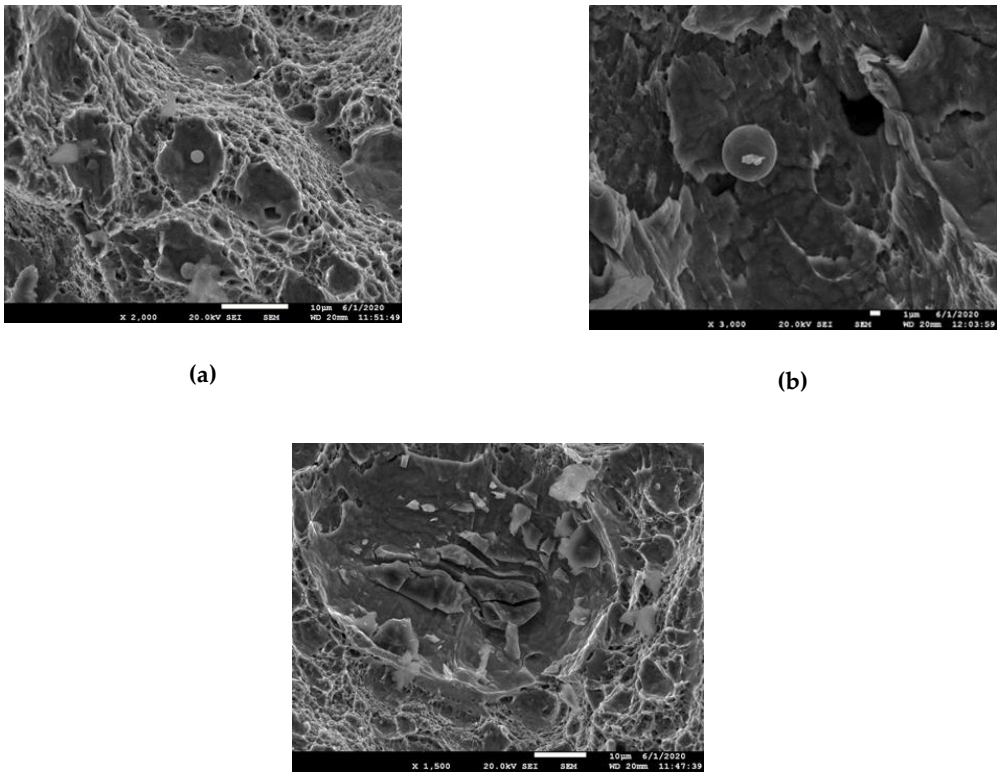

(a) **(b)**

(c)

Figure 8: Fractured surface images of the chessboard family 2 (Samples 13-15)

Preprints (www.preprints.org) | NOT PEER-REVIEWED | Posted: 21 October 2020 doi:10.20944/preprints202010.0435.v1

Figure 8 represents the Chessboard Family 2 displaying a predominantly ductile behaviour with dimples, Figure 8a. In the dimples, spherical non-metallic inclusions are found, Figure 8b as well as regions with residual oxide scales, figure 8c.

Fracture surfaces from the Hexagonal family 1 are shown in Figure 9. The layered structure in Figure 9a shows how the crack propagates along the fusion zone, (flat regions and then works itself across the printed layer) Figure 9b shows the flat surface with easy crack propagation along the fusion zone and figure 9c illustrates the ductile surface at the step where the crack propagates across the built layer. Important to note here is that this type of steps was not as clear nor as visible using the Chessboard strategy, suggesting that the fusion lines were less continuous and possibly exhibited a greater tortuosity that for the hexagonal printing strategy. It should also be noted that unmelted particles also could be found in the hexagonal printing strategy.

Figure 10 shows the fracture surfaces for Hexagonal family 2. In Figure 10a, a mixed-mode fracture surface is seen where the brittle region appears similar to a fusion zone failure. In Figure 10a, a spherical non-metallic inclusion is also seen. In addition to the ductile ridges in the fusion-zone dimples are visible outside the fusion zone. In the ductile areas with dimples, pore-like features are seen with non-metallic residues are seen, figure 10b suggesting that these are not shrinkage porosity but rather a hole after a spherical particle has been torn out. No un-melted particles could be seen in this sample, and ductile ridges and dimples with an appearance in Figure 10c dominated the fracture surface.

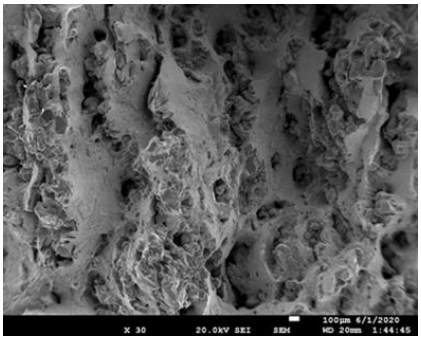

(a)

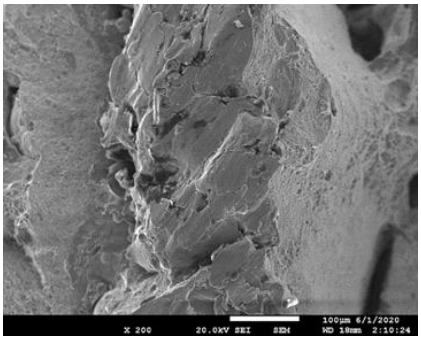

(b)

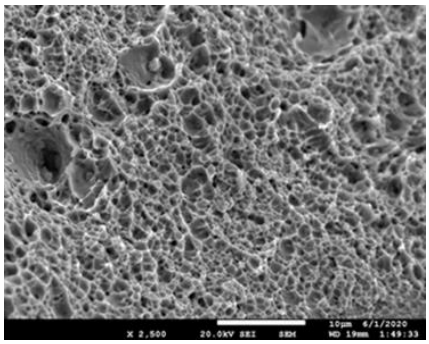

(c)

Figure 9: The fractured surface of the Hexagonal Family 1 (Samples 19-21)

Preprints (www.preprints.org) | NOT PEER-REVIEWED | Posted: 21 October 2020 doi:10.20944/preprints202010.0435.v1

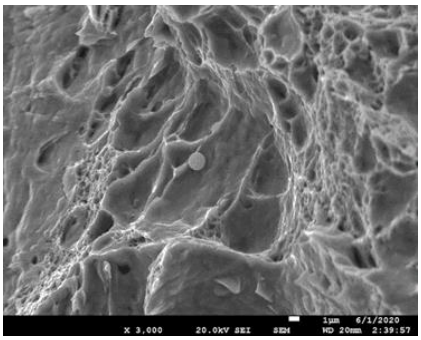

(a)

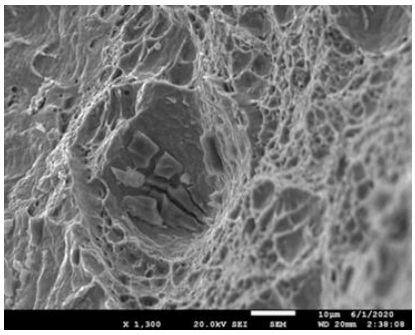

(b)

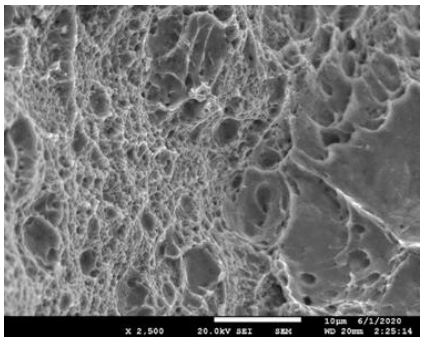

(a)

Figure 10: The fractured surface of the Hexagonal Family 2 (Samples 22-24)

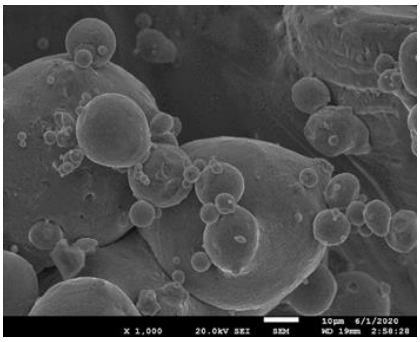

(a)

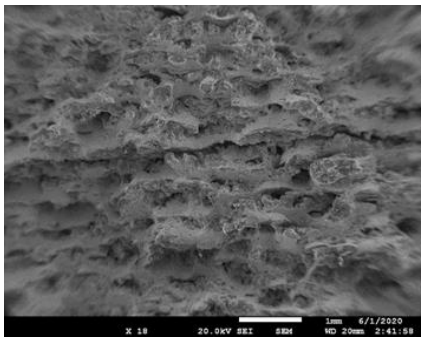

(b)

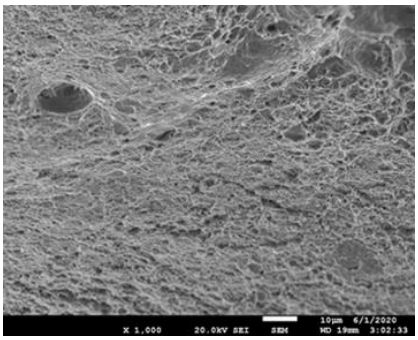

(a)

Figure 11: The fractured surface of the Hexagonal family 3 (Samples 25-27)

Preprints (www.preprints.org) | NOT PEER-REVIEWED | Posted: 21 October 2020 doi:10.20944/preprints202010.0435.v1

Figure 11 represents the fracture surface of the Hexagonal family 3, where unmelted particles, were found, figure 11a. Besides the layered fracture were found as well, figure 11b—the step-like features were found, but not as well-developed in this samples in Hexagonal family 1 that har smaller hatch spacing but a higher scan speed. In figure 11b, there is a large secondary crack visible in the centre of the picture that could have developed into a step, exposing the fusion zone between layer. This did not occur. A possible explanation for this is shown in figure 11c where a bare fusion zone is shown with an appearance resembling dimples. This sample had the lowest scan speed suggesting that low sac speed promotes bonding in the fusion zone.

Figure 12a shows the fracture surface of stripes family 3. In figure 10a, a similar behaviour, as mentioned above, materials processing conditions with unmelted particles, porosity, combined with ductile features such as dimples and ductile ridges are found. Oxide scale could also be detected, figure 12b. Besides, fusion zone driven features could be seen but not as clear as for the Chessboard and the hexagonal scanning strategies families, figure 12c. The tortuosity of the fusions zone appeared higher visually and may be affected by the interlayer rotation choice made.

In figure 13, it is the fractured surface Stripes family 2 are shown. In the absence of continuous fusion-zones, figure 13a, larger dimples and well-developed ductile ridges are found, figure 13b. The dominating defect appeared as oxides, figure 13c. There is a ductile fracture, void nucleation, and some dimples.

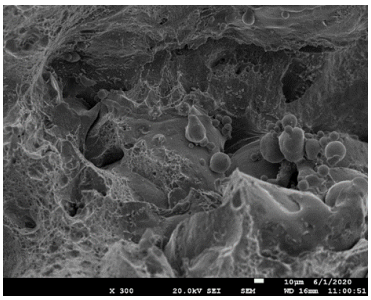

(a)

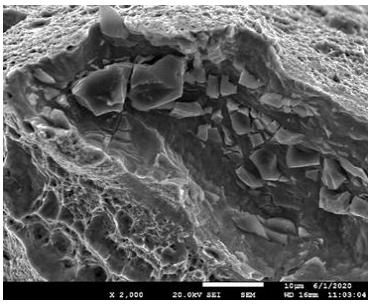

(b)

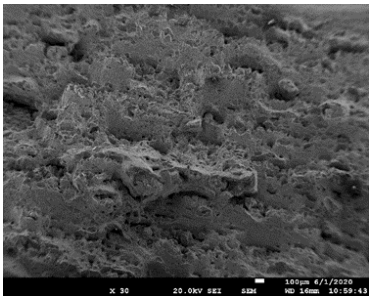

(a)

Figure 12: Stripes Family 3 (Samples 7-9)

Preprints (www.preprints.org) | NOT PEER-REVIEWED | Posted: 21 October 2020 doi:10.20944/preprints202010.0435.v1

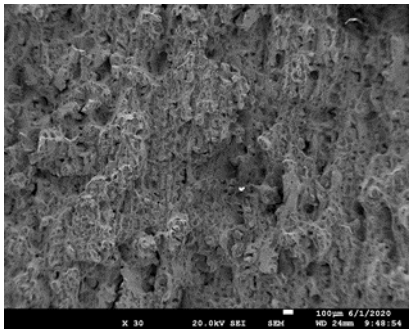

(a)

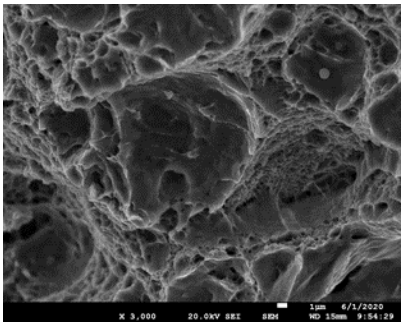

(b)

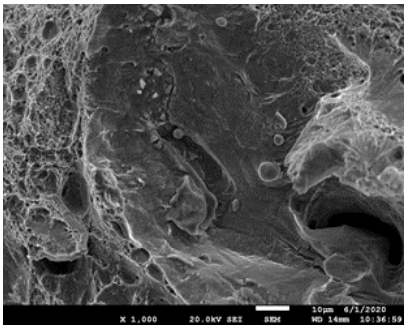

(a)

Figure 13: Stripes family 2 (Samples 4-6)

A comparison between all these fractures, all the printed materials show a microscopically ductile behaviour. Family 2 for all scanning features with intermediate scan speed and hatch spacing combination appeared more ductile. In terms of failure, it appears as if it was dominated by the geometry of the fusion zone where a more complex or tortuous shape reduced the scale and the possible fracture length of the more brittle elements in the fusion zones. The Chessboard offers more fusion-zones as there will be more in-layer fusion zones between the Chessboard squares. Similar features exist in the other families as well but it is only in the Chessboard family where a significant change in the printing orientation exists as both the Stripes family and the Hexagonal families will provide parallel tracks in the fusion zones between the inlayer regions.

5. Conclusions

In the current, the impact fracture strength and crack propagation characteristics of Maraging steel 1.2709 was investigated

Gaseous species such as Oxygen, Hydrogen and Nitrogen were studied. The Hydrogen levels were below detection limits of the equipment and as such, concluded to be non-significant. Nitrogen levels varied between the different printing strategies and process setting, but no correlation could be established with statistical significance. The results for Oxygen were similar, but here the Chessboard pattern appeared to have slightly lower oxygen content, but it was not possible to describe this quantitatively.

In terms of impact strength, the three different printing strategies performed differently with the average impact strength for the Chessboard strategy being superior to the other strategies. Fractography of the Chessboard fracture was different as continuous crack propagation along fusion zones were absent. This was not the case for the Stripes and the Hexagonal strategies where a step-like structure was found. These steps were following the fusion zones. This was furthermore also supported by the Crackarrest force for the different strategies where the Chessboard strategy average Carack arrest forces were higher than for the Stripes and Heaxonal strategies. These three

observations suggest that the Chessboard strategy resulted in a more tortuous fusion zone reducing the mean free path for cracks growing in the fusion zone, being the preferred path of cracking. For all strategies, the influence of the process parameters was similar where a larger hatch spacing promoted impact strength, and a larger interlayer rotation decreased the impact strength.

Author Contributions: Conceptualisation, AEWJ; methodology, ACGHS and HKY; printing software and handling; RS, equipment instrumentation JS, fractography, NEA; supervision, AEWJ.; project administration, AEWJ and RS.; funding acquisition, RS and AEWJ. All authors have read and agreed to the published version of the manuscript.

Funding: This work was done under funding from the Knowledge Foundation under the ToolAddict project contract number 20160327 and the teaching funding at Jönköping University

Acknowledgements: The authors are indebted to Höganäs AB for the supply of the Maraging steel powder for printing under the framework of the Swedish Arena for Additive Manufacturing

Conflicts of Interest: The authors declare no conflict of interest. The funders had no role in the design of the study; in the collection, analyses, or interpretation of data; in the writing of the manuscript, or in the decision to publish the results.

References

1. Kučerová, L.; Zetková, I.; Jandová, A.; Bystrianský, M. Microstructural characterisation and in-situ straining of additive-manufactured X3NiCoMoTi 18-9-5 maraging steel. *Mater. Sci. Eng. A* **2019**, *750*, 70–80, doi:10.1016/j.msea.2019.02.041.
2. Conde, F.F.; Escobar, J.D.; Oliveira, J.P.; Jardini, A.L.; Bose Filho, W.W.; Avila, J.A. Austenite reversion kinetics and stability during tempering of an additively manufactured maraging 300 steel. *Addit. Manuf.* **2019**, *29*, 100804, doi:10.1016/j.addma.2019.100804.
3. Jägle, E.A.; Choi, P.-P.P.; Van Humbeeck, J.; Raabe, D. Precipitation and austenite reversion behavior of a maraging steel produced by selective laser melting. *J. Mater. Res.* **2014**, *29*, 2072–2079, doi:10.1557/jmr.2014.204.
4. Casati, R.; Lemke, J.; Masneri, C.; Vedani, M. Influence of heat treatment condition on properties of 1.2709 maraging steel fabricated by selective laser melting. *World PM 2016 Congr. Exhib.* **2016**.
5. Takata, N.; Nishida, R.; Suzuki, A.; Kobashi, M.; Kato, M. Crystallographic features of microstructure in maraging steel fabricated by selective laser melting. *Metals (Basel).* **2018**, *8*, 1–10, doi:10.3390/met8060440.
6. Ciurana, J.; Hernandez, L.; Delgado, J. Energy density analysis on single tracks formed by selective laser melting with CoCrMo powder material. *Int. J. Adv. Manuf. Technol.* **2013**, *68*, 1103–1110, doi:10.1007/s00170-013-4902-4.
7. de Souza, A.F.; Al-Rubaie, K.S.; Marques, S.; Zluhan, B.; Santos, E.C. Effect of laser speed, layer thickness, and part position on the mechanical properties of maraging 300 parts manufactured by selective laser melting. *Mater. Sci. Eng. A* **2019**, *767*, 138425, doi:10.1016/j.msea.2019.138425.
8. Rivalta, F. Effect of the scanning strategy on the SLM produced 18Ni300 maraging steel, University of Bologna, 2019.
9. Carter, L.N.; Martin, C.; Withers, P.J.; Attallah, M.M. The influence of the laser scan strategy on grain structure and cracking behaviour in SLM powder-bed fabricated nickel superalloy. *J. Alloys Compd.* **2014**, *615*, 338–347, doi:10.1016/j.jallcom.2014.06.172.
10. Jhabvala, J.; Boillat, E.; Antignac, T.; Glardon, R. On the effect of scanning strategies in the selective laser melting process. *Virtual Phys. Prototyp.* **2010**, *5*, 99–109, doi:10.1080/17452751003688368.
11. Valente, E.H.; Gundlach, C.; Christiansen, T.L.; Somers, M.A.J. Effect of scanning strategy during selective laser melting on surface topography, porosity, and microstructure of additively manufactured Ti-6Al-4V. *Appl. Sci.* **2019**, *9*, doi:10.3390/app9245554.

12. Monkova, K.; Zetkova, I.; Kučerová, L.; Zetek, M.; Monka, P.; Daňa, M. Study of 3D printing direction and effects of heat treatment on mechanical properties of MS1 maraging steel. *Arch. Appl. Mech.* **2019**, *89*, 791–804, doi:10.1007/s00419-018-1389-3.
13. Viswanathan, U.K.; Dey, G.K.; Sethumadhavan, V. Effects of austenite reversion during overageing on the mechanical properties of 18 Ni (350) maraging steel. *Mater. Sci. Eng. A* **2005**, *398*, 367–372, doi:10.1016/j.msea.2005.03.074.
14. Da Costa E Silva, A.L.V. Non-metallic inclusions in steels - Origin and control. *J. Mater. Res. Technol.* **2018**, *7*, 283–299, doi:10.1016/j.jmrt.2018.04.003.
15. Surian, E.; Trotti, J.; Boniszewski, T. Effect of oxygen content on charpy V-notch toughness in 3% Ni steel SMA weld metal. *Weld. J.* **1992**, *71*, 263.
16. Terashima, S.; Bhadeshia, H.K.D.H. Changes in toughness at low oxygen concentrations in steel weld metals. *Sci. Technol. Weld. Join.* **2006**, *11*, 509–516, doi:10.1179/174329306X113299.
17. Elmi Hoseini, S.R.; Arabi, H.; Razavizadeh, H. Improvement in mechanical properties of C300 maraging steel by application of VAR process. *Vacuum* **2008**, *82*, 521–528, doi:10.1016/j.vacuum.2007.08.008.
18. Sreenivasan, P.R. Instrumented impact testing - Accuracy, reliability and predictability of data. *Trans. Indian Inst. Met.* **1996**, *49*, 677–696.
19. Box, G.E.P.; Hunter, J.S.; Hunter, W.G. *Statistics for Experimenters: Design, Innovation, and Discovery*; 2nd ed.; John Wiley and Sons Inc.: Hoboken, New Jersey, 2005; ISBN 978-0471718130.